Int. J. Electrochem. Sci., 15 **(2020)** 11606 – 11622, doi: 10.20964/2020.11.39

International Journal of
ELECTROCHEMICAL
SCIENCE
www.electrochemsci.org

Effect of Carbon Content and Microstructure on the Diffusion of Hydrogen in Low Carbon Steels

J. G. Arenas-Salcedo, J. G. Godínez-Salcedo[*], *J. L. González-Velázquez, J. M. Medina- Huerta*

Instituto Politécnico Nacional, Escuela Superior de Ingeniería Metalúrgica, Departamento de Ingeniería Metalúrgica y Materiales, México
[*]E-mail: drgodinez@hotmail.com

Received: 24 April 2020 / *Accepted:* 24 July 2020 / *Published:* 30 September 2020

In this work, the electrochemical permeation technique proposed in the ASTM-G148-97 Ed 2011 standard was used to determine the maximum oxidation current density, i_{max}; breakthrough time; t_b, effective hydrogen diffusion coefficient, D_{eff}; and surface hydrogen concentration, C_H^0, for several API 5L steels. The results show that steels with a carbon content of less than or equal to 0.052 %wt and a ferritic-bainitic microstructure have higher D_{eff} and i_{max} values than steels with a higher carbon content and a ferritic-pearlitic microstructure, while the C_H^0 and tb parameters show a clear tendency to decrease when the microstructure changes from ferritic-pearlitic to ferritic-bainitic. The D_{eff} values obtained in this work are consistent with published data, both in terms of their magnitude and in relation to the effects of carbon content and microstructure.

Keywords: hydrogen diffusion, diffusion equations, Electrochemical Permeation Technique.

1. INTRODUCTION

It is well known that hydrogen (H) diffuses into carbon steels under a variety of circumstances, including cathodic charging, sour gas corrosion, etc. [1]. The hydrogen diffusivity is a function of the lattice parameter and the microstructure [2-6], as well as on the content of trapping sites such as grain boundaries, dislocations [7] and microvoids among others [8-12]. The role of carbon content on H diffusion is indirect, and the most well-known fact is that high carbon steels are prone to hydrogen embrittlement and hydrogen-induced cracking (HIC) [13], implying that the carbon content might affect the diffusivity of H in steel. Regarding the effect of second phases on H diffusion, it has been reported that pearlite, martensite/austenite, which are hard constituents, have a high H trapping efficiency, while ferrite and acicular ferrite, which are softer, tend to resist HIC [14-16]. As reported by G.T. Park [17], steels with ferrite + bainite microstructures have better resistance to HIC than steels

containing ferrite + martensite microstructures. Li et al. [18] found that steels containing polygonal ferrite and granular bainite + acicular ferrite microstructures did not exhibit HIC.

To better understand the role of carbon content and microstructure on the characteristics of H diffusion in low carbon steels, in this work, a group of steels with bainite + ferrite microstructures and another group with pearlite + ferrite microstructures, both with varying fractions of pearlite and bainite as well as carbon content, were laboratory tested by the ASTM G-148-97 electrochemical permeation technique. The results are compared to those obtained from similar works related to hydrogen diffusion in different API Steels [13, 19].

It is generally accepted that a steel with a low sulfur and low volume fraction of inclusions is more resistant to HIC because there are less sites for H trapping [20]. On the contrary, steels with elongated manganese sulfur and aluminum oxide, aluminum-calcium-silicon oxide are more susceptible to HIC, as reported by Hara et al. [21] and Hejazi et al. [22].

In general, the following processes can be distinguished in a metal-hydrogen system: (i) entry, (ii) diffusion, and (iii) entrapment in microstructural defects and/or hydride formation [1]. The efficiency of H entry is characterized by the solid solution concentration just below the surface [23], while the diffusion is described by Fick's laws, where the diffusion coefficient is affected by the microstructure [10, 24].

Among the various electrochemical tests used for measuring H uptake in metals, the Electrochemical Permeation of Hydrogen test described by Devanthan was used [25]. This test allows one to determine the following parameters: effective diffusivity $\boldsymbol{D_{eff}}$, breakthrough time $\boldsymbol{t_b}$, representing the time required for H to pass through the metallic sample or permeation membrane, the maximum permeation current density, $\boldsymbol{i_{max}}$, which represents the Faradaic equivalent of H that is steadily oxidized in an oxidation cell, and $\boldsymbol{C_H^0}$, which is the concentration of H in the surface of the corroding surface in a charging cell.

It has been stated that when $\boldsymbol{C_H^0}$ is below a limit value, $\boldsymbol{C_H^{lim}}$, the interstitial lattice positions are the common path for H diffusion, but that when $\boldsymbol{C_H^0}$ exceeds $\boldsymbol{C_H^{lim}}$, the HIC cracks begin to propagate, consuming part of the diffusing H [25-26]. When the concentration of H is sufficiently high to cause embrittlement, the flux of H that passes through the metal increases with time, and, after reaching a steady-state, the current drops due to the consumption of the H ions in the solution [26].

In a sour environment, the reactions that take place in the charging cell during the corrosion process are as follows:

$Fe(S) \rightarrow Fe\ (ac) + 2e^-$ Anodic Reaction

$2H^+ + 2e^- \rightarrow 2H\ (ad)$ Cathodic Reaction

Both reactions are carried out at the same rate, so the total reaction is given by

$2Fe + 2H^+ \rightarrow 2Fe^{2+} + H_2$

If chemical spices such as arsenic, selenium, sulfur or phosphorus, called "Poisons", are present in the solution, the formation of molecular hydrogen is retarded or inhibited [1]. Therefore, the metal surface will be saturated with H atoms, which are capable of diffusing into the metal.

The reaction carried out on the oxidation side is given by

$H^0 - 1e^- \rightarrow H^+$

Using the first Fick's law, the hydrogen flux through the membrane, J_{ss}, can be calculated in terms of the maximum permeation current, i_{max}, at the steady state [23,27-28] by equation (1):

$$J_{ss} = -D_{eff}\left(\frac{\partial C}{\partial x}\right)_{x=L} = \frac{i_{max}}{nF} \quad (1)$$

Where J_{ss} is the hydrogen permeation flux at steady state (atoms/cm^2 s), D_{eff} is the coefficient of effective hydrogen diffusion (cm^2/s), i_{max} is the maximum permeation current density at steady state (μA/cm^2), n is the number of transferred electrons, F is Faraday's constant (96485.33 Coulomb/mol), L is the plate thickness (cm) and $(\partial C/\partial x)_{x=L}$ is the concentration gradient.

Fick's Second Law describes the concentration of the species that diffuses as a function of position and time in a non-steady state. The equation describing the diffusion in a single direction through the lattice is expressed as follows:

$$\frac{\partial C(x,t)}{\partial t} = \frac{\partial}{\partial x} D_{eff} \frac{\partial}{\partial x}[C(x,t)] \quad (2)$$

Where $C(x,t)$ is the concentration of hydrogen in the lattice as a function of position and time (mol/cm^3). By solving the differential equation (2), the following equation is obtained [27-28]:

$$D_{eff} = \frac{L^2}{15.3(t_b)} \quad (3)$$

Thus, the value of D_{eff} can be obtained from the measured value of t_b (s) for a given L (cm) for the membrane.

On the other hand, the concentration of H in the inner side of the charged side C_H^0 (mol/cm^3) can be obtained from the solution of Fick's First Law equation, becoming [27-28]

$$C_H^0 = \frac{i_{max} L}{D_{eff} nF} \quad (4)$$

In this work, testing coupons for API 5L steels with different microstructures were tested to evaluate their susceptibility to H diffusion in steels. The electrochemical charging conditions were performed without coating for samples exposed to an acidic solution (pH ≈ 0); the pH value was low enough to supply H ions by corrosion reactions without an applied cathodic current to reproduce real-life operating conditions of components exposed to sour environments where these factors are not controlled [28].

2. EXPERIMENTAL PROCEDURE

The electrochemical permeation tests consisted of placing a sample or permeation membrane between a double electrochemical cell, as schematically depicted in Figure 1 [25]. The H entry mechanism is a cathodic reaction, where an aqueous electrolyte, such as sulfuric acid (H_2SO_4), carries the H ions. An oxidizing agent composed of 0.1 M sodium hydroxide (NaOH) is placed into the second electrochemical cell (detection cell or oxidation cell), and the oxidation current is measured. This current is the faradic equivalent of the H flow through the membrane exit surface.

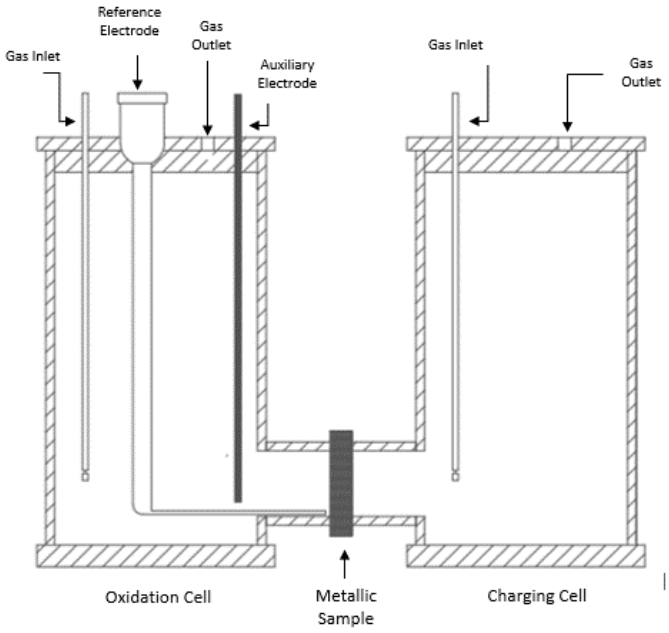

Figure 1. Electrochemical Double Cell.

The samples were fabricated from two steels with an extra low carbon content and a bainitic microstructure of API 5L X-52 and X-70 specification and from two steels with a carbon content greater than 0.1 %wt and a ferrite-pearlite microstructure of API 5L X-60 and X-65 specification. The test blocks in the form of rectangular plates with a height of 4.0 cm, width of 3.0 cm and thickness of 0.40 cm were cut by a mechanical saw with a coolant to avoid modification of the microstructure, and then machined to the required dimensions. A commercial steel SAE 1018 was used in the preliminary potentiodynamic anodic polarization test because it has a similar chemical composition with pearlitic steels and was used as a reference to establish the passivation current densities.

The elemental chemical analysis was carried out by using a spark spectrometry technique. For the metallographic analysis, a sample of each steel was prepared by grinding to 2000 SiC sandpaper followed by polishing with alumina in a suspension of 0.3 μ and 0.05 μ to achieve a mirror-finish.

The inclusion content and the microstructure were characterized by optical metallography with an Olympus GX51 image analyzer according to the ASTM E1382 - 97(2015), ASTM E45-18A, ASTM E1122 and ASTM E407 standards. The specimens were etched with Nital 2% reagent to reveal the microstructure.

Potentiodynamic anodic polarization tests were performed according to the ASTM G-5-94 (2007) [29] standard procedures. Electrochemical permeation tests were performed as per the ASTM G-148-2011 [27] standard. Both tests were carried out using a Potentiostat-Galvanostat model 263 AE&G from Princeton Applied Research, equipped with PowerSuite software for data acquisition and processing.

To perform the polarization and permeation tests, the test coupons were polished on both sides with 600 grit SiC sandpaper, and then cleaned with acetone, alcohol and distilled water to remove any

residue of dirt or grease. The samples were placed between the chambers of the double electrochemical cell, and then tightly tightened with screws and fastening joints to avoid leakage. The oxidation cell was filled with 500 ml of a 0.1 M NaOH solution prepared with high purity reagents. Nitrogen gas was bubbled for 10 minutes to deaerate the solution and displace the oxygen. The reference electrode (Calomel Saturated Electrode KCl) was placed through a Luggin capillary, and a compact graphite bar was used as the auxiliary electrode. This experimental set up is shown in Figure 1.

The preliminary potentiodynamic anodic polarization tests were performed as a suggestion of the ASTM G148 permeation standard, under the conditions of the oxidation cell, to determine the control potentials (≈300 mV) for the background oxidation current densities (passive).

Once the double cell was assembled and connected to the potentiostat, the permeation tests were started, applying the control potentials (≈300 mV) against the Ecorr in the oxidation cell, which were obtained in the preliminary potentiodynamic anodic polarization tests. The background oxidation current densities (passive) were allowed to stabilize in the oxidation cell for 1 hour, and then, 500 ml of a 2 M H_2SO_4 + 0.1 M Na_2SO_4 solution was added to the charging cell, along with 30 ml of Na_2S 0.1 M as a poisonous ion, resulting in pH = 0. This charging cell solution as well as the oxidation cell solution was maintained with a constant bubbling of N_2 gas. The test temperature was maintained at 21 ± 0.2 ° C. Under these conditions, the oxidation current density was observed to increase rapidly after the transfer time $\mathbf{t_b}$; the charging of hydrogen into the samples lasted 35,000 s.

3. RESULTS

3.1 Chemical compositions of the tested steels

The chemical compositions of the tested steels are shown in Table 1. The API 5L X-70 and X-52 steels were identified as **B**, standing for "bainite", while the rest of the steel samples were identified as **P**, standing for pearlite.

Table 1. Chemical composition of the steel samples used in experiments, (% wt).

X-70 B				L (average thickness) = 0.31 cm						
C	Si	Mn	P	S	Cu	Al	Cr	Mo	Ni	V
0.023	0.245	0.950	0.036	0.05	0.219	0.089	0.114	0.015	0.182	0.021
		Ti	Nb	Co	W	B	Fe			
		0.021	0.102	0.043	0.077	0.0001	Bal			
X-52 B				L (average thickness) = 0.32 cm						
C	Si	Mn	P	S	Cu	Al	Cr	Mo	Ni	V
0.052	0.208	0.708	0.012	0.0462	0.321	0.041	0.07	0.011	0.033	0.013
		Ti	Nb	Co	W	B	Fe			
		0.004	0.037	0	0.005	0	bal			
X-60 P				L (average thickness) = 0.37 cm						

C	Si	Mn	P	S	Cu	Al	Cr	Mo	Ni	V
0.187	0.262	1.38	0.086	0.144	0.0108	0.0038	0.118	0.005	0.055	0.002
		Ti	Nb	Co	W	B	Fe			
		0.0031	0.003	0.0125	0.0182	0.0027	bal			
X-65 P				L (average thickness) = 0.38 cm						
C	Si	Mn	P	S	Cu	Al	Cr	Mo	Ni	V
0.24	0.076	1.175	0.078	0.0692	0.0032	0.010	0.049	0.016	0.029	0.01
		Ti	Nb	Co	W	B	Fe			
		0.001	0.014	0.011	0.015	0	bal			

3.2 Microstructure

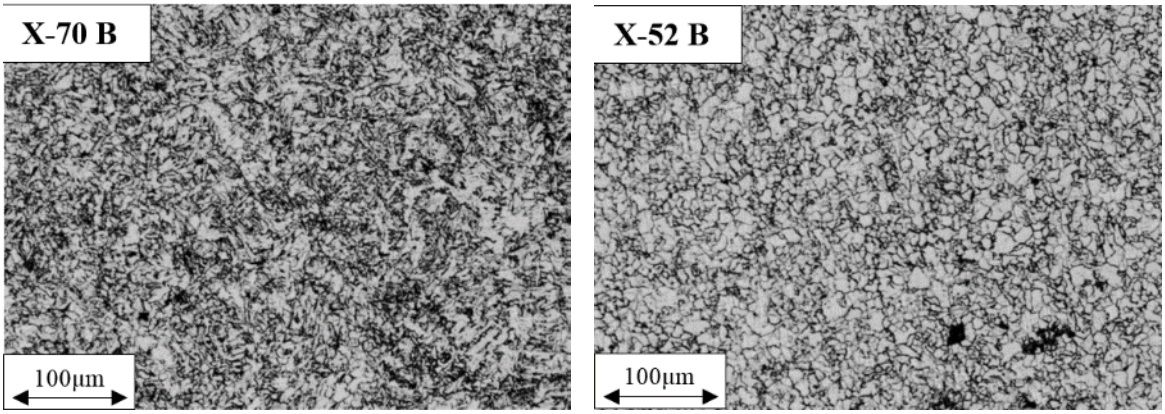

Figure 2. Microstructure of steel samples with an upper bainite microstructure. Optical microscope, etched with Nital 2%.

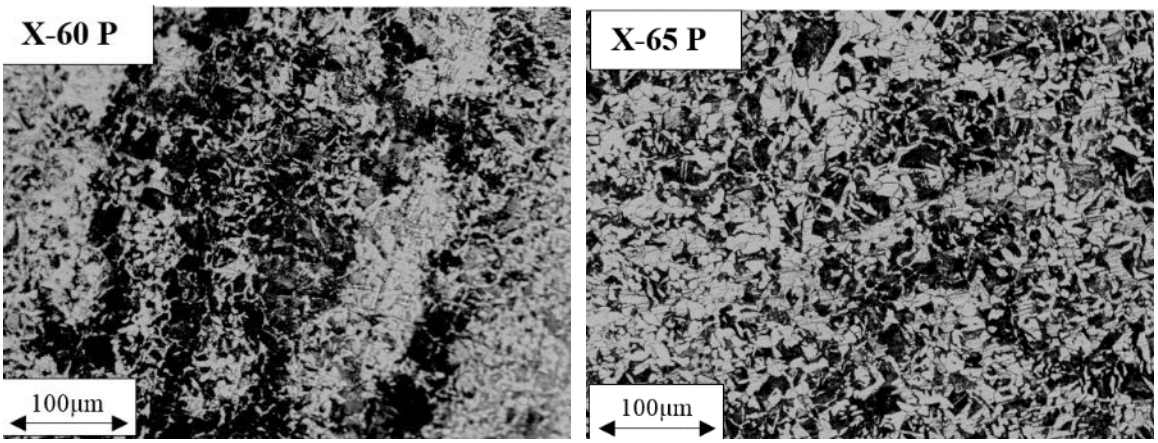

Figure 3. Microstructure of steel samples with a ferrite-pearlite microstructure. Optical microscope, etched with Nital 2%.

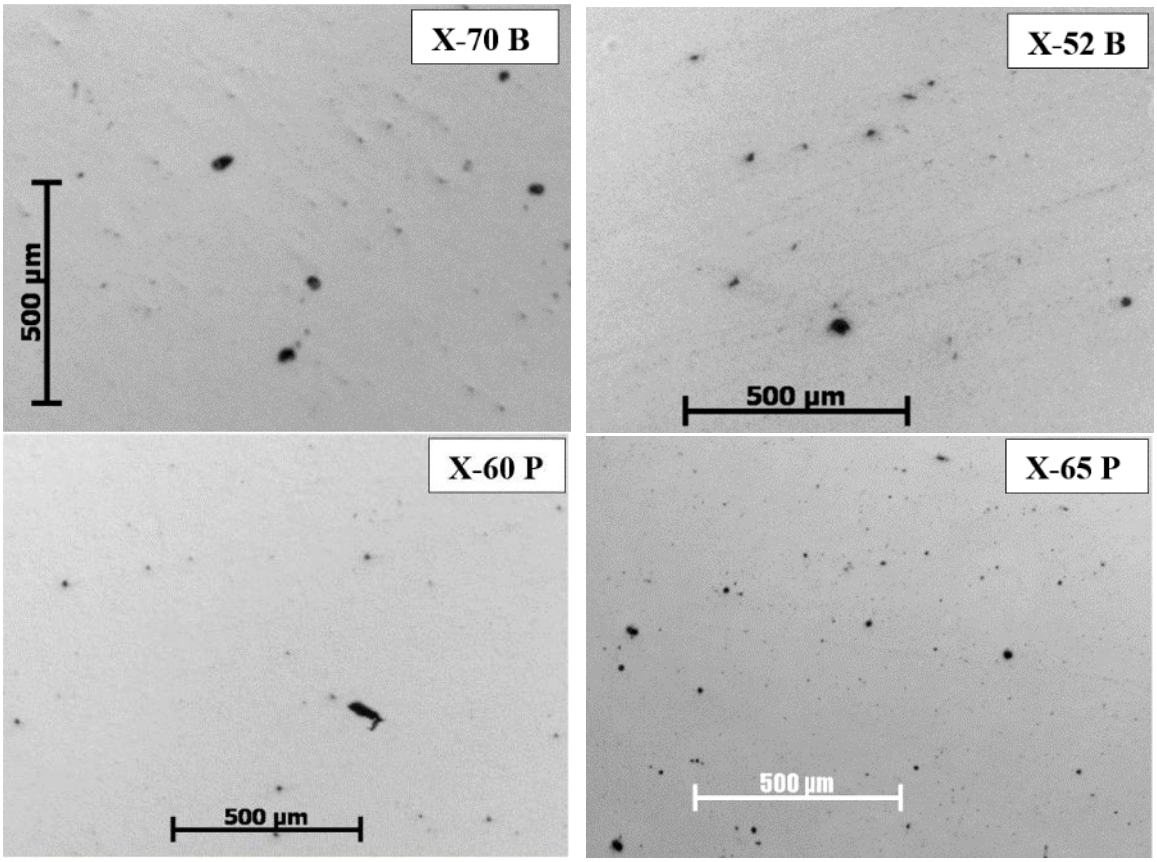

Figure 4. Inclusions of steel samples. Optical microscope, as polished.

The surface microstructures of the tested steels are shown in Figures 2 and 3. The microstructures of the X-70 B and X-52 B steels consist of upper bainite. The non-metallic inclusions are Type I globular oxides, fine series, as shown in Figure 4. The microstructures of the X-60 P and X-65 P steels consist of a ferrite matrix with polygonal colonies of lamellar pearlite; the X-60 P contains pearlite segregation zones, as shown in Figure 3. The non-metallic inclusions were Type II manganese sulfides, fine series, as shown in Figure 4. The inclusion content vs average size of inclusions is shown in Figure 5. Table 2 shows the size and amount of non-metallic inclusions. Table 3 shows the phase fraction present and the average grain size.

Table 2. Size and amount of non-metallic inclusions.

Steel	% Objects/area (µm^2) (Avg.)	Length (µm)	Width (µm) (Avg.)	Area (µm^2) (Avg.)
X-60 P	3.55 x10^{-5}	6.98	3.24	22.68
X-65 P	2.65 x10^{-5}	7.02	3.67	25.85
X-52 B	2.22 x10^{-5}	5.16	2.90	14.97
X-70 B	1.14 x10^{-5}	3.00	4.64	13.95

The following Table shows the phases and its fraction present in each steel and average grain size.

Table 3. Average grain size and second phase percentage

Steel	%Phases		Average Grain Size ASTM (μm)		
	α-Fe	2nd Phase	Sup	Long	Trans
X-52 B	97.01	2.97	10.1 (10.842)	10.0 (11.225)	10.2 (10.473)
X-70 B	88.07	11.9	9.81 (11.989)	9.80 (12.031)	9.86 (11.783)
X-60 P	59.66	40.3	9.30 (14.307)	9.21(14.760)	9.32 (14.208)
X-65 P	68.48	31.5	9.10(15.334)	8.89 (16.490)	9.01 (15.765)

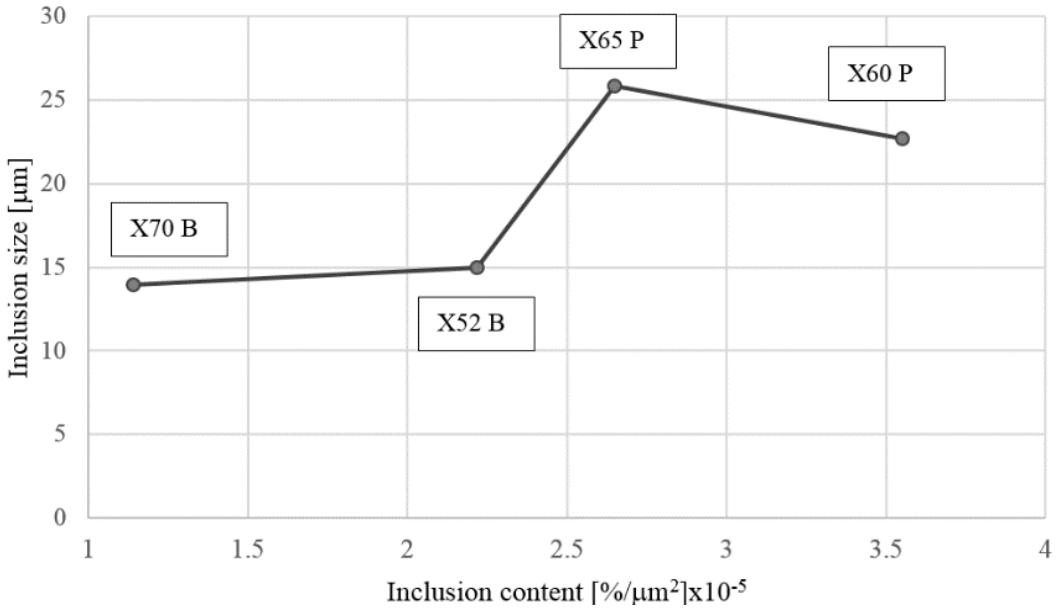

Figure 5. Inclusion comparative sizes in the tested steels.

SEM images of the microstructure are shown in Figures 6 and 7, which show that all steels have α-ferrite as the main constituent and the second phase of the X-70 B and X-52 steels is bainite, while X-60 and X-65 steels contain a lamellar cementite as the second phase.

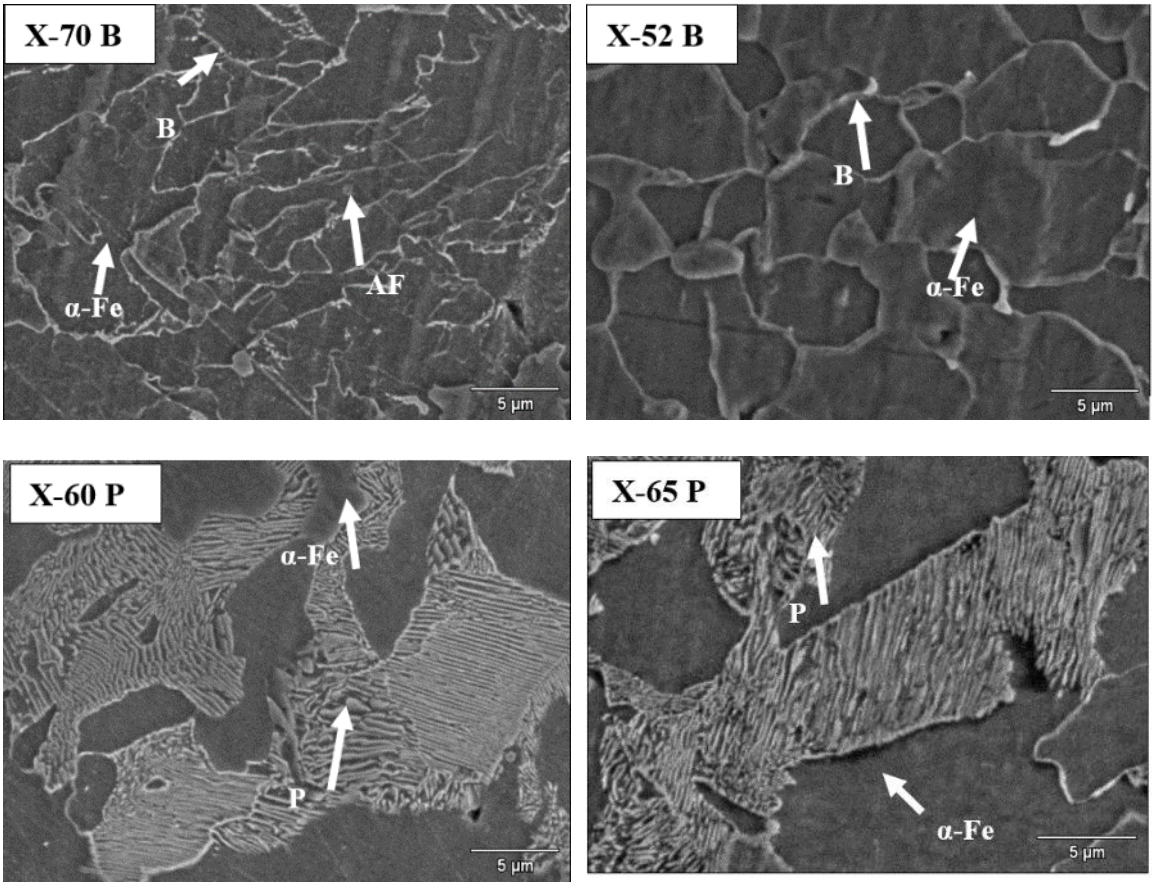

Figure 6. SEM Images of the sample miscrostructure (B:Bainite, AF: Acicular Ferrite, α-Fe Ferrite, P: Pearlite).:

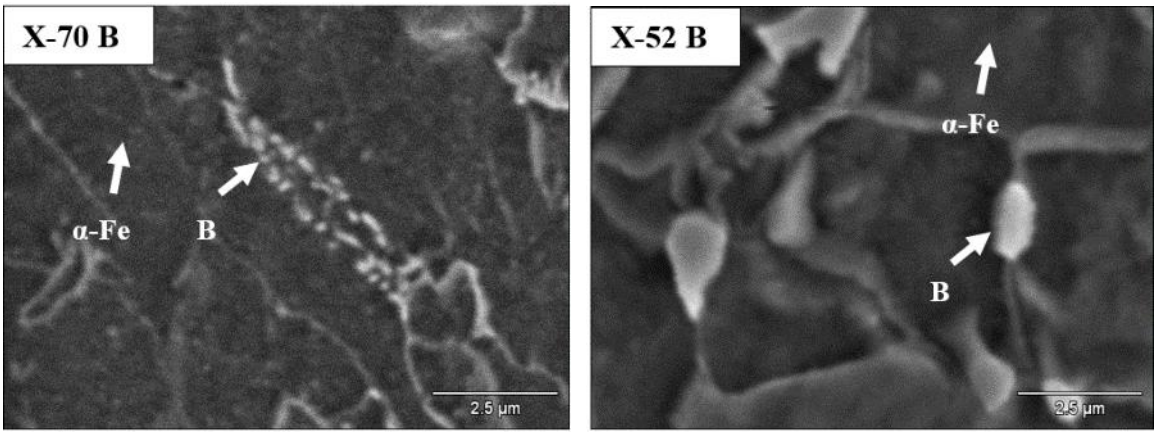

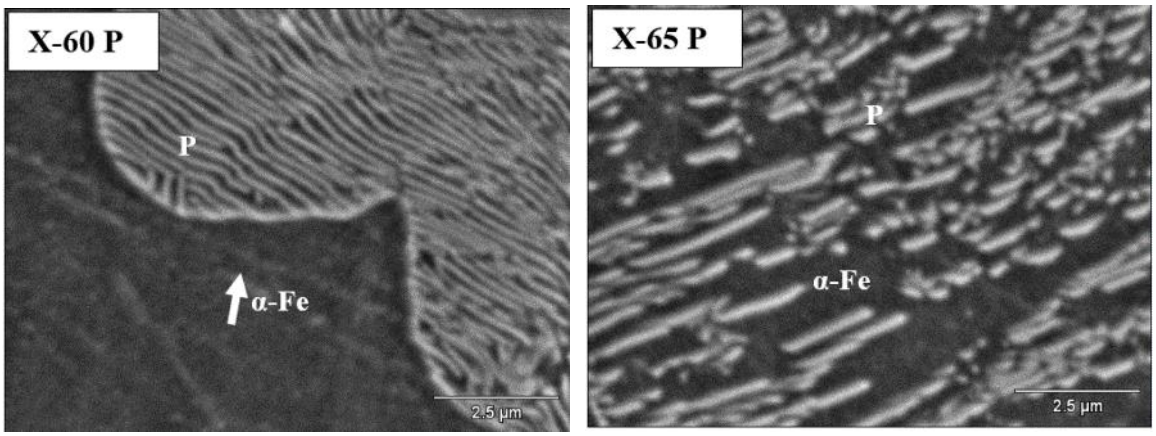

Figure 7. Close-up SEM images of the sample miscrostructure (B:Bainite, α-Fe Ferrite, P: Pearlite).:

3.3 Electrochemical tests

3.3.1 Potentiodynamic anodic polarization test

Figure 8 shows the graph obtained from a potentiodynamic anodic polarization test carried out using an oxidation cell for a commercial steel SAE 1018, where the control potential (≈300 mV) and the corresponding background oxidation current density (passive), (≈ 5µA / cm^2) can be observed.

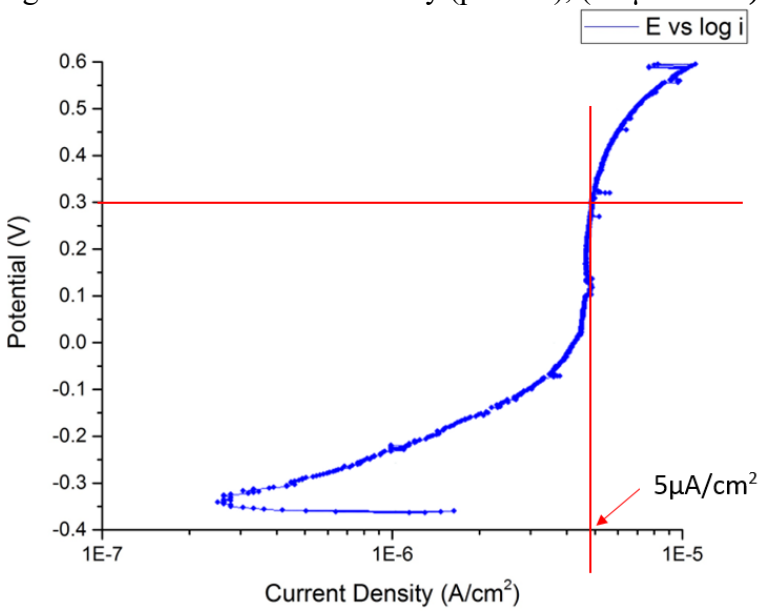

Figure 8. Solution Potentiodynamic anodic polarization curve: oxidation cell filled with 0.1 M NaOH solution. Control potential (≈300 mV) for the background oxidation (Passive) current density (≈ 5µA/cm^2).

The graphs obtained for X-70, X-52, X-60 and X-65 steels were similar to those obtained for SAE 1018 steel; when applying control potentials of 300 mV, background oxidation current densities

(passive) for the steels were 1.1 μA / cm^2, 0.48 μA / cm^2, 1.39 μA / cm^2 and 0.54 μA / cm^2, respectively, Figure 9 and Table 4.

3.3.2 Permeation Tests

The results obtained from the hydrogen permeation tests were similar to those shown in Table 4, and the corresponding permeation plots are presented in Figure 9, which are similar to those reported by Elboujdaini et al [28].

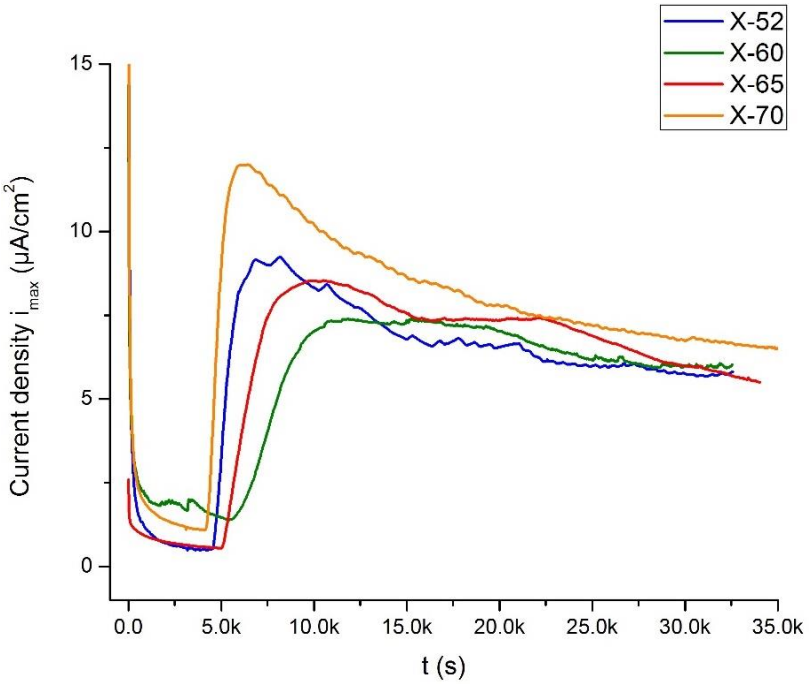

Figure 9. Hydrogen permeation plots of the API-X70, API-X52, API-X65 and API-X60 Steels

Regarding the electrochemical tests carried out for steel membranes, typical graphs obtained after three repetitions are shown in Figure 9. The i_{max} and D_{eff} values for bainitic steels are higher than those obtained for perlitic steels, as shown in the Figures 9, 10 and Table 4. The observed deviation among the tests is attributed to the microstructural differences between the samples, which is consistent with other works [8-9, 19, 30].

The background current density in the hydrogen permeation tests is low and relatively stable compared to the currents measured when hydrogen enters the sample.

Table 4. Parameters obtained from hydrogen permeation tests.

STEEL	% C	L (cm)	t_b (s)	D_{eff} *E^{-06} (cm^2/s)	Background Current Density (μA/cm^2)	i_{max} (μA/cm^2)	C_H^O (μmol/cm^3)
X-70 B	0.023	0.315	580	11.2	0.48	10.81	3.15
X-52 B	0.052	0.32	650	10.3	1.39	9.15	2.94
X-60 P	0.187	0.377	1850	5.02	0.54	5.98	4.65
X-65 P	0.24	0.382	1400	6.81	1.11	7.51	4.36

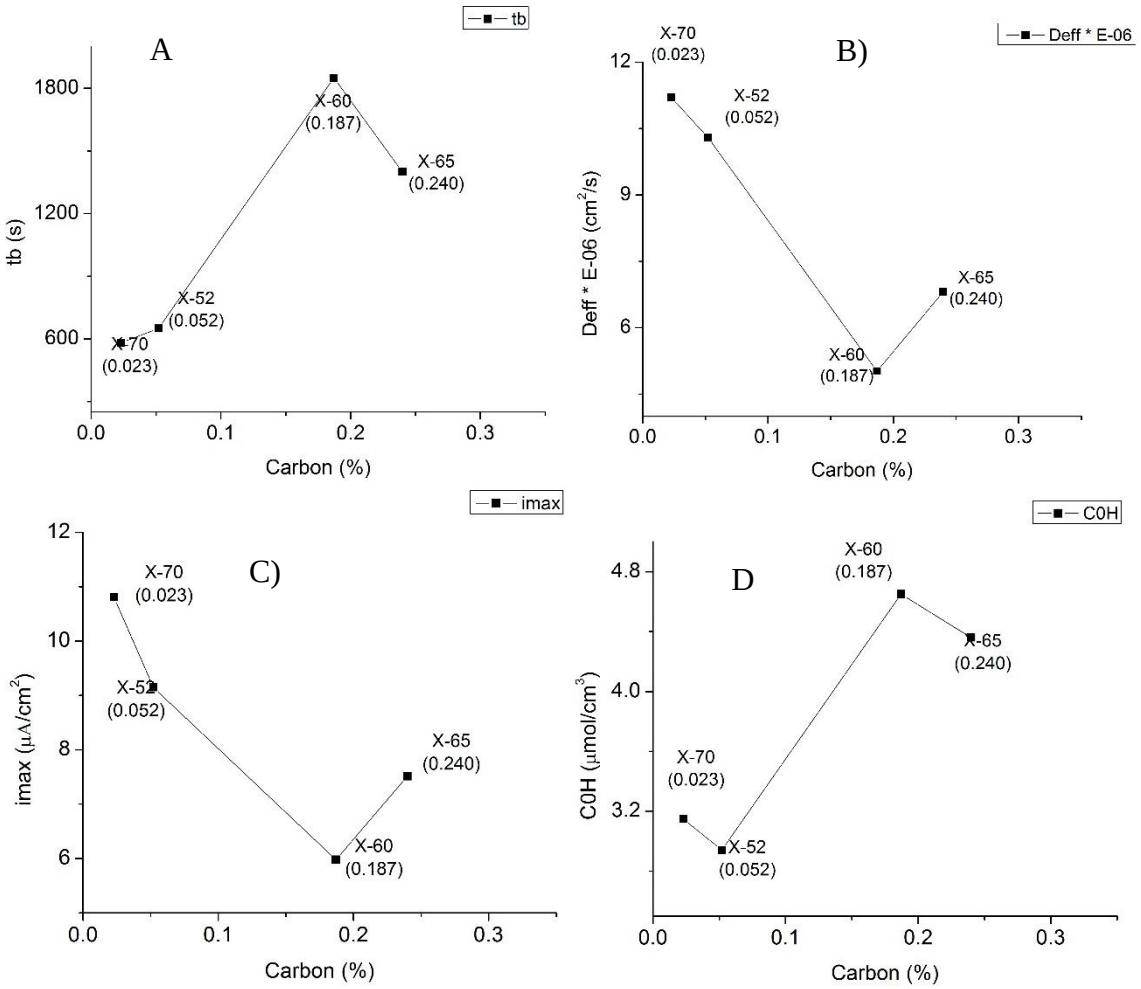

Figure 10. Main parameters for the tested Steels vs %Carbon Content

Figure 10 A) shows that steels with a higher carbon content have a higher t_b with respect to those steels with a lower carbon content. Likewise, it can be noted in Figure 10 B) that the diffusion coefficient D_{eff} decreases with carbon content. This behavior is attributed to the fact that diffusivity is greater in the ferrite phase than in the pearlitic phases, as reported in reference [31] The same occurs with i_{max} since the H atoms move easily trough the lattice and produce higher values of i_{max}, as can be

observed in Figure 10 C). In Figure 10 D), it is observed that the surface hydrogen concentration C_H^0 is higher for higher carbon content, which presents a pearlitic microstructure. This behavior is attributed to the amount of hydrogen that is retained in the ferrite / cementite interface [31-32]. In summary, it can be said that steels with higher carbon content tend to retain a greater amount of hydrogen in the surface. Therefore, such steels are expected to be more susceptible to HIC.

4. DISCUSSION

4.1. Effect of chemical composition

The steels studied here show significant differences in chemical composition, as shown in Table 1. Bainitic steels show lower amounts of Mn and S, which makes bainitic steels less likely to form MnS inclusions that are known to act as irreversible H traps [8-9, 19, 33-34].

It has been reported that the addition of Nb, Ti and V rounds up the grain boundaries and restricts grain growth in addition to helping other elements (C, N, S and P) become solid solution during hot rolling. The formation of nitrides and carbides of Mo, V, Nb, Cr and Ti tends to form precipitates, which are beneficial for the entrapment of H and improving the mechanical strength [34-35]. These elements are present in greater amounts in X-70 and X-52 steel samples than in steels with higher carbon content. The addition of Cu also improves the HIC resistance in steels and reduce the risk from H damage [36]. In this work, the bainitic steels connote more Cu than the pearlitic steels, and, consequently, have a lower C_H^O.

However, it is considered that the amounts of these elements in the tested specimens are not sufficient to exert an effect greater than that of the carbon content.

4.2. Effect of carbon content

From Table 4 and Figures 10 B) 10 C), it is observed that the steels with lower carbon content (B steels) show a higher D_{eff} and higher i_{max} in comparison to steels with a higher carbon content (P steels). It is interesting to note that among the B steels, higher D_{eff} and i_{max} values were found for a lower carbon content, (8.03 % and 15.35% variation, respectively), but, in the P steels, the opposite effect was observed, i.e., the higher the carbon content, the higher the D_{eff} and the lower the i_{max}.

The effect of carbon content on the diffusion parameters t_b and C_H^O appears to be higher for pearlitic steels, as the higher values correspond to the X-60 P. This behavior is attributed to pearlite banding and segregation, as shown in Figure 3, where both B steels show lower values for these parameters.

These results indicate that the effect of the carbon content on the diffusion of hydrogen in steel may be more significant at high carbon contents. This can be attributed to the fact that a greater number of interstitial sites is occupied by carbon atoms in the ferrite lattice. In opposition, the depletion of carbon from the lattice to form carbides in the bainite microstructures increases the

diffusivity. While in ferrite-pearlite steels, only the carbon content in excess of the equilibrium solubility in ferrite forms cementite flakes that constitute part of the pearlite.

4.3. Effect microstructure

The results in Table 4 and Figure 10 show a clear effect of the microstructural condition on the diffusion parameters of carbon steel, with higher $\boldsymbol{D_{eff}}$ and $\boldsymbol{i_{max}}$ values found for the bainitic steels. However, this effect is concomitant with the effect of carbon content, as discussed below.

Low carbon bainitic steels are fabricated by controlled thermomechanical processes, where the eutectoid reaction is suppressed by rapid cooling at temperatures below the critical Ac_1 temperature (727 °C), leaving the austenite as a metastable solid solution. Then, the combination of heat and plastic deformation promotes the precipitation of a dispersion of fine carbides and the transformation of austenite into a stable form of ferrite, which, in conjunction, constitutes the bainite [35, 37-38]. Figures 6 and 7 show the phase morphology of the bainitic steels. It has been established that α-Fe is more sensitive to the entry of hydrogen; so, the ferritic-bainitic steels have a greater diffusivity of hydrogen than the ferritic-pearlitic steels, as shown in Table 3. This is because the bainitic steels contain more α-Fe (X-70 B: 88.07% and X-52 B: 97.01%). Moreover, it has been reported that steels with higher carbon content show a smaller diffusivity and higher superficial hydrogen concentration $\boldsymbol{C_H^O}$ [8, 31, 39].

The effect of microstructure on the diffusion of H in steel can also be explained by the number of hydrogen trapping sites that are present in the microstructure. As suggested by Araujo [39] and Reyes [40], pearlite is an effective trapping site for H, leading to $\boldsymbol{D_{eff}}$ to decrease and $\boldsymbol{t_b}$ to increase with respect to bainitic steels that have a ferrite matrix, which provides a free path for H passage. In addition to the fact that the dispersion of spherical carbides are not an efficient trapping site [41-42], it is also likely that pearlite bands act as barriers for H diffusion, resulting in the X-60 P steel showing the lowest $\boldsymbol{D_{eff}}$ and $\boldsymbol{i_{max}}$ values in combination with the highest $\boldsymbol{t_b}$ and $\boldsymbol{C_H^O}$ shown by the B steels tested in this work.

The effect of the grain size can be observed in Figures 9, 10 B) and 10 C), where the bainitic steels with a small grain size (see Table 3) show higher $\boldsymbol{D_{eff}}$ and $\boldsymbol{i_{max}}$. This is attributed to a greater grain boundary area, as reported by Cheolho Park [42] and Rogéiro Augusto [43], which better distributes the diffusible hydrogen trapped in the grain boundary, reducing the amount of hydrogen trapped in the steel.

It was also observed that $\boldsymbol{D_{eff}}$ is clearly affected by $\boldsymbol{tb}$, which is a function of the path that the hydrogen atom follows through the lattice. This is why the steel with the highest amount of non-metallic inclusions (X60 P) and banded pearlitic microstructure shows the largest $\boldsymbol{tb}$ and the highest $\boldsymbol{C_H^O}$ since the nonmetallic inclusions act as irreversible traps for H [31].

4.4. Comparison with other works

To validate our results and to determine if similar effects for carbon content and microstructure have been observed by others, the results of this work were compared to those obtained in similar

studies reported in the literature. The results from Araujo et al. [39] were obtained for ferrite-pearlite steels, similar to the P steels tested in this work. API 5L-X80 steel with a carbon content of 0.084 %wt showed D_{eff} = 3.37 E-06 cm^2s^{-1}, while an API 5L-X60 steel with a carbon content of 0.12 %wt showed D_{eff} = 2.11 E-06 cm^2s^{-1}. These values are within the same range of D_{eff} values obtained here.

The results obtained here also coincide with those reported by Luu and Wu [3], who analyzed the effect of carbon content and microstructure on the value of D_{eff}, obtaining the results listed in Table 5.

Table 5. Results for the D_{eff} obtained by Luu and Wu [3].

Steel	%C	D_{eff} *E^{-06} cm^2/s	C_H^O µmol/cm^3
Tempered	0.05	10.5	0.44
S45 C	0.45	2.96	1.18

These results show that at higher carbon content, D_{eff} is lower and C_H^O increases. This behavior is consistent with the tendency observed here.

Regarding the hydrogen concentration in the steel, M. Liu et al. [30] showed that C_H^O increases with carbon content and time. AISI 1018 with 0.13-0.2 % C showed lower values for C_H^0 than AISI 4340 with 0.38-0.43 %C. These data are very similar to those obtained here.

Another study by S. L. I. Chan [38] showed that the hydrogen concentration increases as the amount of ferrite/pearlite increases, as observed in the tests described here.

Finally, Gye-Won Hong [31] showed that the steady state of H permeation flux decreases as the pearlite area increases, and the apparent diffusivity of hydrogen in carbon steel decreases as the α-Fe-cementite increases. These results are shown in Table 6.

Table 6. Results for the D_{app} obtained by Gye-Won Hong [31].

Steel	**%C**	D_{app} $x10^{-3}x\ \exp(-\frac{26.79kJmol^{-1}}{RT})(cm^2s^{-1})$
0.12C Steel	0.12	7.201
0.49C Steel	0.49	6.163

5. CONCLUSIONS

Although no electrochemical charging was applied to the charging cell, the results and the data obtained here match well with those reported in the literature, especially the D_{eff} and C_H^O values obtained for the same type of steels. Therefore, it is expected that bainitic steels with a fine grain size and lower nonmetallic inclusion content will have a lower C_H^O than pearlitic steels.

Steels with a low carbon content show higher effective diffusion coefficients, D_{eff}, and higher maximum oxidation currents, i_{max}, in comparison to steels with higher carbon content.

Despite the non-clear tendency of the diffusion parameters t_b and C_H^O, the effect of the carbon content on these parameters was observed. The highest and lowest t_b and C_H^O values were obtained for steel with a carbon content of 0.187 % wt and 0.023 % wt, respectively.

The steels with a bainitic microstructure showed the highest D_{eff} and i_{max} values in comparison to ferrite-pearlite steels. This effect was concomitant with the effect of carbon content and is attributed to the free paths available for hydrogen passage and the number and efficiency of hydrogen trapping sites. Bainitic steels appear to provide easier paths for hydrogen passage, while their spherical carbides do not act as efficient hydrogen trapping sites, in opposition to ferritic-pearlitic steels, where pearlite bands may act as physical barriers for hydrogen diffusion, in combination with a high efficiency of pearlite to act as a hydrogen trapping site.

The values of D_{eff} obtained in this work are consistent with published data, both in terms of the magnitude, as well in relation to the effect of carbon content and microstructure.

ACKNOWLEDGMENTS

The authors wish to thank the Grupo de Analisis de Integridad de Ductos (GAID) for their economic support and for providing experimental materials, laboratory equipment and scholarship funding. The authors are grateful to Consejo Nacional de Ciencia y Tecnologia (CONACYT) for the grants associated with this work. The authors express their gratitude for the use of the Corrosion Laboratory of the Metallurgical and Materials Engineering Department of the Instituto Politécnico Nacional (DIMM-ESIQIE-IPN).

References

1. M. G. Fontana, Corrosion Engineering, McGraw-Hill, (2005) Michigan University, U. S. A.
2. A. R. Troiano, *Trans. AIME*, 52 (1960) 54.
3. W. C. LUU and J. K. WU, *Corros. Sci.*, 38 (1996) 239.
4. N. R. Moody, A. W. Thompson, R. E. Ricker, G. S. Was, and R. H. Jones, Hydrogen Effects on Material Behavior and Corrosion Deformation Interactions, Wyoming, U. S. A., 2003.
5. M. Cabrini, O. Cogliati and S. Moffi, *La Metalurgia Italiana*, 3 (2003) 13.
6. M. L. Luppo and J. Ovejero García, *Corros. Sci*., 32 (1991) 1125.
7. S. Wang, M. L. Martin, P. Sofronis, S. Ohnuki, N. Hashimoto and I. M. Robertson, *Acta Mater*., 69. (2014) 275.
8. A. J. Haq, K. Muzaka, D. P. Dunne, A. Calka, and E. V. Pereloma, *International Journey of Hydrogen Energy*, 38 (2013) 2544.
9. F. M. Bolzoni, E. Fallahmohammadi, G. Re, G. Fumagalli, M. Ormellese and L. Lazzari, Electrochemical Investigation of Hydrogen Diffusion in Pipeline Steels, NACE - International Corrosion Conference Series. (2013).
10. V. P. Ramunni, T. Coelho and P. E. V. Miranda, *Mater. Sci. Eng*., A, 435-436 (2006) 504.
11. E. Ohaeri, U. Eduok and J. Szpunar, *Engineering Failure Analysis* 96 (2019) 496.
12. M. A. Mohtadi-Bonab, J. A. Szpunar and S. S. Razavi-Tousi, *Engineering Failure Analysis* 33 (2013) 163.
13. M. A. Mohtadi-Bonab and H. Ghesmati-Kucheki, Important Factors on the Failure of Pipeline Steels with Focus on hydrogen Induced Cracks and Improvement of Their Resistance: Review Paper, *Met. Mater.* Int., 2019.
14. X. Shi, W. Yan, W. Wang, L. Zhao, Y Shan And K. Yang, *J. Iron. Steel Res. Int*., 22 (2015) 937.

15. S. U. Koh, H. G. Jung, K. B. Kang, G. T. Park and K. Y. Kim, *Corrosion*, 64 (7) (2008) 574.
16. X. Shi, W. Yan, W. Wang, L. Zhao, Y. Shan, and K. Yang, *Acta Metall. Sin. (Engl. Lett.)*, 28 (7) (2015) 799.
17. G. T. Park, S. U. Koh, H. G. Jung and K. Y. Kim, *Corros. Sci*., 50 (7) (2008) 1865.
18. J. Li, X. Gao, L. Du and Z. Liu, *J. Mater. Sci. Technol*., 33 (2017) 1504.
19. E. Ohaeri, U. Eduok and J. Szpunar, Hydrogen related degradation in pipeline steel: A Review, *International Journal of Hydrogen Energy* (2018)
20. K. M. M. Rahman, M. A. Mohtadi Bonab, R. Ouellet, J. Szpunar and N. Zhu, *International Journal of Pressure Vessels and Piping* 173 (2019).147.
21. T. Hara, H. Asahi and H. Ogawa, *Corrosion* 60 (2004) 1113.
22. D. Hejazi, A. Haq, N. Yazdipour, D. Dunne, A. Calka, F. Barbaro and E. Pereloma, *Mater. Sci. Eng.* A 551 (2012) 40.
23. G.H. Geiger and D.R. Portier, Transport Phenomena in Metallurgy, Addison-Wesley Publishing Company, 2nd Ed, (1980) U. S. A.
24. K. Takai and R. Watanuki, *ISIJ Int*., 43 (4) (2003) 520.
25. M. A. V. Devanathan and Z. Stachurski, *Proc. R. Soc. London, Ser*. A, 270 (1962) 90.
26. J. O. M. Bockris, Modern Electrochemistry 2A: Fundamentals of Electrodics v. 2a, Springer, (2008) U. S. A.
27. ASTM-G 148- 97 (Reaproved 2011), Standard Practice for Evaluation of Hydrogen Uptake, Permeation, and Transport in Metals by an Electrochemical Technique.
28. M. Elboujdaini, V.S. Sastri and R.W. Revie, *Corrosion Engineering*, 50 (8) (1994) 636.
29. ASTM G-5-94 (2004) Standard Reference Test Method for Making Potentiodynamic Anodic Polarization Measurements.
30. M. A. Liu, P. E. J, Rivera-Díaz-del-Castillo, J. I. Barraza-Fierro, H. Castaneda and A. Srivastava, *Mater. Des*., 167 (2019).
31. G. Hong and J. Lee, *J. Mater. Sci*., 18 (1983) 271.
32. A. A. Kholodnyi, Y. I. Mastrosov, M. Y. Mastrosov and S. V. Sosin, *Metallurgist*, 60 (Nos. 1–2) (2016) 54.
33. F. Huang, J. Liu, Z. J. Deng, J. H. Cheng, Z. H. Lu and X. G. Li, *Mater. Sci. Eng*. A, 527 (2010) 6997.
34. Z. Shirband, M. R. Shishesaz and A. Ashrafi, *Phase Transitions*, 84 (2011) 924.
35. R. Abbaschian and R. E. Reed-Hill, Physical Metallurgy Principles, CENGAGE LEARNING; 4th Ed, (2008), Stamford, U. S. A.
36. X. Shi, W. Yan, W. Wang, Y. Shan and K. Yang, *Mater. Des*., 92 (2016) 300.
37. J. Apraiz Barreiro, Tratamientos Térmicos de los Aceros, S.L. Cie Inversiones Editoriales Dossat-2000, 10ª Ed. (2002) Madrid, España.
38. S. L. I. Chan and J. A. Charles, *Materials Science and Technology*, 2 (9) (1986) 956.
39. B. A. Araújo, J. A. Palma, E. O. Vilar and A. A. Silva, *Información Tecnológica*, 22 (6) (2011) 129.
40. F.A. Reyes Valdes, "Efecto de la Microestructura en las Condiciones de flujo de Hidrógeno a Través de aceros al Carbono, Tesis de Doctorado, 2004, Universidad de Nuevo león, México.
41. P. Rivera, V. Ramunni and P. Bruzzoni, *Corros. Sci*., 54 (2012) 106.
42. C. Park, N. Kang and S. Liu, *Corros. Sci*., 128 (2017) 33.
43. R. A. Carneiro, R. C. Ratnapuli and V. Lins, *Mater. Sci. Eng*. A, 357 (2003) 104.